nature physics

Article

https://doi.org/10.1038/s41567-025-02822-y

A metallic room-temperature d-wave altermagnet

Received: 7 August 2024

Accepted: 10 February 2025

Published online: 18 March 2025

Check for updates

Bei Jiang[1,2,12], Mingzhe Hu[1,2,12], Jianli Bai[1,2,12], Ziyin Song[1,2,12], Chao Mu[1,2,12], Gexing Qu[1,2], Wan Li[1,3], Wenliang Zhu[4], Hanqi Pi[1,2], Zhongxu Wei[1], Yu-Jie Sun[5,6,7], Yaobo Huang[8], Xiquan Zheng[9], Yingying Peng[9], Lunhua He[1,10,11], Shiliang Li[1,2,11], Jianlin Luo[1,2], Zheng Li[1,2] ✉, Genfu Chen[1,2] ✉, Hang Li[1] ✉, Hongming Weng[1,2,11] ✉ & Tian Qian[1] ✉

Altermagnetism is a recently discovered unconventional magnetic phase that is characterized by time-reversal symmetry breaking and spin-split band structures in materials with zero net magnetization. Recently, spin-polarized band structures and a vanishing net magnetization were observed in semiconductors MnTe and $MnTe_2$, confirming this unconventional magnetic order. Metallic altermagnets offer advantages for exploring physical phenomena related to low-energy quasiparticle excitations and for applications in spintronics because the finite electrical conductivity of metals allows direct manipulation of the spin current through the electric field. We demonstrate that KV_2Se_2O is a metallic room-temperature altermagnet with d-wave spin-momentum locking. Our experiments probe the magnetic and electronic structures of this compound and reveal a highly anisotropic spin-polarized Fermi surface and the emergence of a spin-density-wave order in the altermagnetic phase. These characteristics suggest that KV_2Se_2O could be a helpful platform for high-performance spintronic devices and for studying many-body effects coupled with unconventional magnetism.

Altermagnetism describes a new type of long-range magnetic order beyond conventional ferromagnetism and antiferromagnetism[1–5]. Historically, altermagnets were classified as antiferromagnets, as both exhibit zero net magnetization. Recent theoretical studies have found that non-relativistic spin-splitting can exist in certain magnets with zero net magnetization, even without spin–orbit coupling (SOC), leading to the concept of altermagnetism[1–11]. In the language of symmetry, an enhanced symmetry group called a spin space group[12–19] classifies magnetic order by the allowed symmetry operations connecting opposite-spin sublattices. In conventional antiferromagnets, opposite-spin sublattices can be connected by inversion or translation operation, whereas ferromagnets have only one spin sublattice, which does not require any symmetry operation. By contrast, altermagnets essentially require rotation or a mirror operation to connect opposite-spin sublattices[1,2,6,7], resulting in momentum-dependent spin-splitting in electronic band structures.

[1]Beijing National Laboratory for Condensed Matter Physics and Institute of Physics, Chinese Academy of Sciences, Beijing, China. [2]University of Chinese Academy of Sciences, Beijing, China. [3]School of Physical Science and Technology, Ningbo University, Ningbo, China. [4]School of Physics and Information Technology, Shaanxi Normal University, Xi'an, China. [5]Department of Physics and Guangdong Basic Research Center of Excellence for Quantum Science, Southern University of Science and Technology, Shenzhen, China. [6]Quantum Science Center of Guangdong-Hong Kong-Macao Greater Bay Area, Shenzhen, China. [7]Institute of Advanced Science Facilities, Shenzhen, China. [8]Shanghai Synchrotron Radiation Facility, Shanghai Advanced Research Institute, Chinese Academy of Sciences, Shanghai, China. [9]International Center for Quantum Materials, School of Physics, Peking University, Beijing, China. [10]Spallation Neutron Source Science Center, Dongguan, China. [11]Songshan Lake Materials Laboratory, Dongguan, China. [12]These authors contributed equally: Bei Jiang, Mingzhe Hu, Jianli Bai, Ziyin Song, Chao Mu. ✉e-mail: lizheng@iphy.ac.cn; gfchen@iphy.ac.cn; hang.li@iphy.ac.cn; hmweng@iphy.ac.cn; tqian@iphy.ac.cn

https://doi.org/10.1038/s41567-025-02822-y

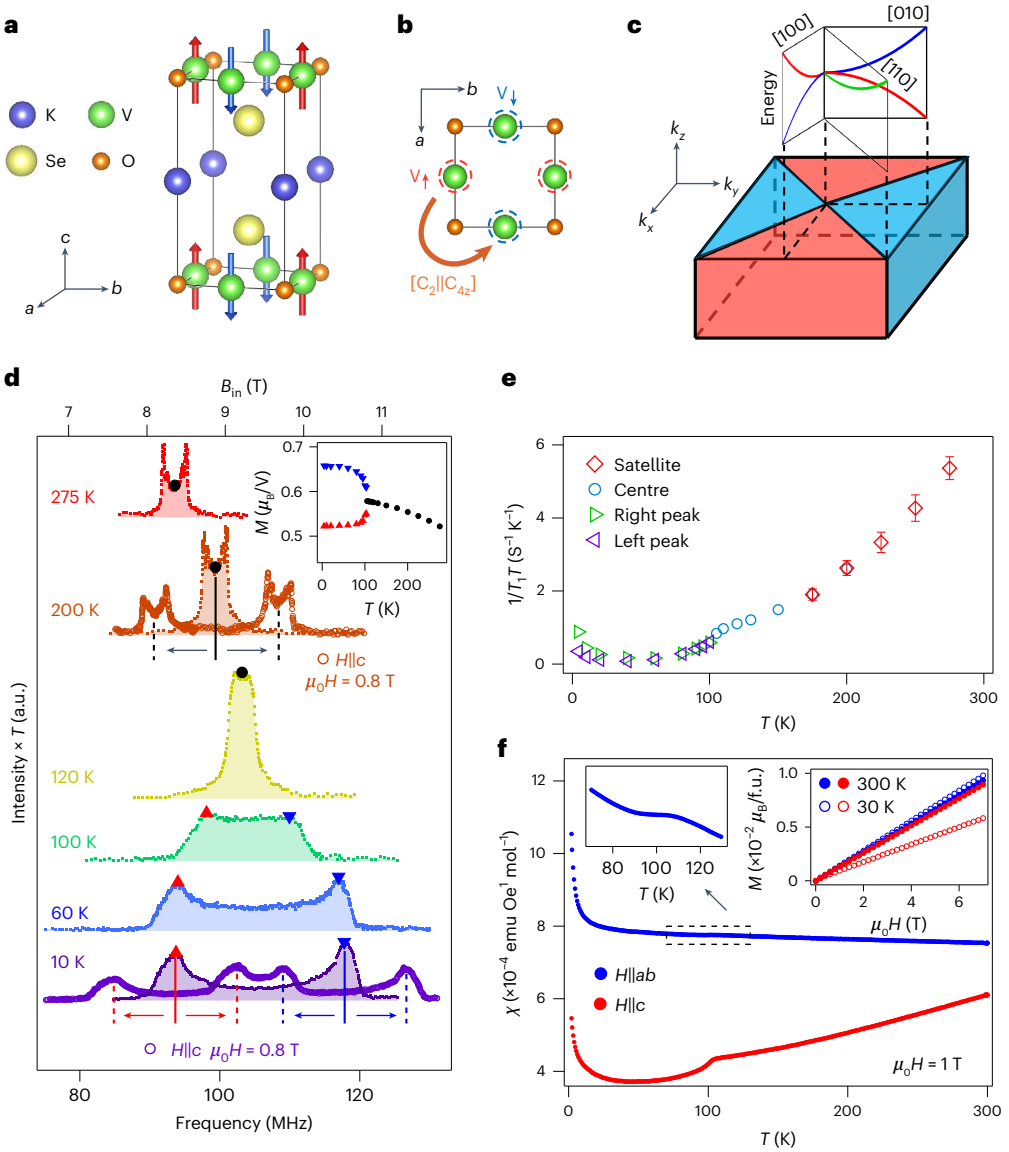

Fig. 1 | Magnetic structure characterization. a, Crystal structure and magnetic structure of KV_2Se_2O. Red and blue arrows indicate the up and down spins of the V atoms. **b**, Top view of the V_2O plane. Red and blue dashed circles surrounding the V atoms denote the up and down spins. Opposite-spin sublattices are connected by the $[C_2||C_{4z}]$ operation. **c**, Schematic for the sign of spin-splitting in the 3D BZ of KV_2Se_2O. Schematic spin-polarized bands are plotted at the top. Red, blue and green curves represent spin-up, spin-down and spin-degenerate bands. **d**, ^{51}V frequency-sweep NMR spectra at different temperatures. B_{in} indicates the internal magnetic field corresponding to the frequency. Dots are the spectra measured at zero field. Empty circles are the spectra at 10 and 200 K measured under $\mu_0H = 0.8$ T with the magnetic field H parallel to the c axis. Inset, magnetic moments M of the V atoms as a function of temperature T. **e**, Spin-lattice relaxation rate $1/T_1T$ of ^{51}V extracted from **d**, where T_1 is the spin-lattice relaxation time. Above the SDW transition temperature, $1/T_1T$ was measured at the third satellite peak on the right (red diamonds) and at the centre of the spectra (blue circles). Error bars are the standard deviation of the least squares fitting, as detailed in Methods. Below the transition temperature, $1/T_1T$ was measured at the highest positions of the broad left (purple triangles) and right peaks (green triangles). **f**, Temperature-dependent magnetic susceptibilities (χ) under $\mu_0H = 1$ T with magnetic fields parallel and perpendicular to the c axis. Top left inset, zoom-in of χ marked by the black dashed box. Top right inset, field-dependent magnetization at 30 and 300 K with magnetic fields parallel and perpendicular to the c axis, where f.u. represents formula unit.

The same symmetry operation connects opposite-spin sub-bands in reciprocal space[1,2,6]. Unlike the spin-splitting induced by the Rashba–Dresselhaus interaction[20,21] in non-magnets lacking inversion symmetry and the Zeeman interaction in ferromagnets, the non-relativistic symmetry operation acts as a crucial aspect in the momentum-dependent spin-splitting in altermagnets[1,2]. The combination of spin-split band structures and zero net magnetization in altermagnets has immense application potential, ranging from spintronics to quantum information processing[22–26].

Although symmetry analyses of spin structures have predicted numerous altermagnet candidates[1,2], only a few have been experimentally verified. Recent spin- and angle-resolved photoemission spectroscopy (SARPES) experiments have revealed momentum-dependent spin-splitting in the band structures of MnTe (ref. 27) and $MnTe_2$ (ref. 28), which is solid evidence for the existence of the altermagnetic phase. These two materials are semiconductors with a global bandgap at the Fermi level (E_F)[12,13,29,30], which limits their potential applications in spintronics. The metallic candidates CrSb and RuO_2 have attracted widespread attention[31–41]. Owing to the C_3 symmetry of the spin sublattices in CrSb and MnTe, opposite-spin channels have the same group velocities in all directions, leading to an unpolarized current. Despite the observation of the anomalous Hall effect and spin

https://doi.org/10.1038/s41567-025-02822-y

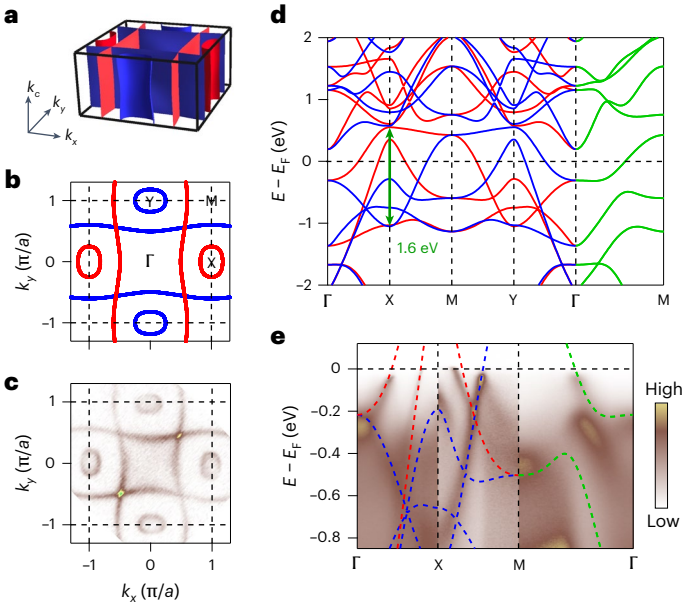

Fig. 2 | Electronic structure of the altermagnetic configuration. a, Calculated spin-resolved FSs in the 3D BZ. Red and blue surfaces are spin-up and spin-down FSs. **b**, Calculated spin-resolved FSs in the $k_z = 0$ plane. Red and blue curves are spin-up and spin-down FSs. **c**, ARPES intensity plot at E_F measured at 120 K with $h\nu = 67$ eV, showing FSs in the k_x–k_y plane. Black dashed lines in **b** and **c** indicate the BZ boundary. **d**, Calculated spin-resolved band structure without SOC along high-symmetry lines. Red, blue and green curves are spin-up, spin-down and spin-degenerate bands. **e**, ARPES intensity plot measured at 20 K with $h\nu = 67$ eV, showing band dispersions along Γ–X–M–Γ. The spectra along Γ–X and M–Γ are the sum of the data collected under linear horizontal and linear vertical polarizations (Extended Data Fig. 7). Dashed curves are the calculated bands, which are shifted upward by 90 meV to better match the experimental data.

current and torque in RuO_2 (refs. 37–40), there remains controversy about whether it is non-magnetic or magnetic[41–43].

In this work, we identified a metallic altermagnet KV_2Se_2O with a magnetic ordering temperature well above room temperature. The momentum-dependent spin-splitting across E_F reached 1.6 eV, one of the highest values reported for altermagnets. This altermagnetic order is characterized by d-wave exchange splitting, which is a magnetic counterpart to unconventional d-wave superconductivity. The extreme anisotropy of the spin-polarized Fermi surfaces (FSs) with C_2 symmetry results in notable differences in the group velocities of opposite-spin channels. This enables the generation of a highly polarized electric current and a giant spin current, which are crucial for achieving high-performance spintronic devices. Another spin-density-wave (SDW) order arises from perfect FS nesting below 100 K, which is a unique opportunity for studying the interplay of many-body effects coupled with unconventional magnetism.

Magnetic structure of altermagnetic order

KV_2Se_2O has a tetragonal layered crystal structure with space group $P4/mmm$ (Fig. 1a)[44]. The V_2O plane has an anti-CuO_2 structure, with Se atoms located directly above and below the centre of the V_2O square. The V_2Se_2O layers are separated by K atomic layers. X-ray and neutron diffraction data are refined well using space group $P4/mmm$, confirming the high crystallinity of the samples (Extended Data Fig. 1).

The well-defined peaks in the ^{51}V nuclear magnetic resonance (NMR) spectra reveal that the magnetic moments of the V atoms form long-range order in the measured temperature range (Fig. 1d). Above 100 K, the spectra at zero field have a single set of peaks with quadrupole splitting, which indicates that the magnetic moments have a uniform magnitude. Below 100 K, the zero-field spectra split into two sets of peaks with different central frequencies, suggesting an SDW transition that results in magnetic moments with two distinct magnitudes. The inset of Fig. 1d shows that the magnitudes of the magnetic moments decrease slightly with increasing temperature, indicating that the magnetic ordering temperature is well above room temperature. Above 100 K, the NMR spin-lattice relaxation rate ($1/T_1T$) gradually decreases with decreasing temperature (Fig. 1e), reflecting the suppression of spin fluctuations in the magnetically ordered phase. The drop near 100 K is attributed to further suppression of spin fluctuations because of the formation of another SDW order. Below 50 K, $1/T_1T$ has an upturn, suggesting enhanced spin fluctuations at low temperatures. The temperature dependence of $1/T_1T$ is well consistent with the magnetic susceptibility data in Fig. 1f, as $1/T_1T$ is proportional to the dynamic magnetic susceptibility.

Under a magnetic field of 0.8 T along the c axis, the NMR spectra at 200 K split into two sets of peaks with similar intensities, and the central frequency shifts by ±0.8 T, indicating that the spins with equal populations align oppositely along the c axis. The NMR data reveal a collinear compensated magnetic order, which is essential for altermagnets. Based on these results, we propose a magnetic structure with altermagnetic order, as illustrated in Fig. 1a. Nearest-neighbour V atoms in the V_2O plane have opposite spins aligned along the c axis. This magnetic structure is supported by the ARPES results, which show excellent agreement with the calculations based on this structure (Figs. 2 and 3). The opposite-spin sublattices cannot be connected by a translation or inversion operation. Instead, they are connected by the spin group symmetry $[C_2||C_{4z}]$ (Fig. 1b), where C_2 represents the non-relativistic spin-space operation to flip the magnetic moments and C_{4z} represents a fourfold rotation along the z axis in real space. This altermagnetic order leads to momentum-dependent spin-splitting

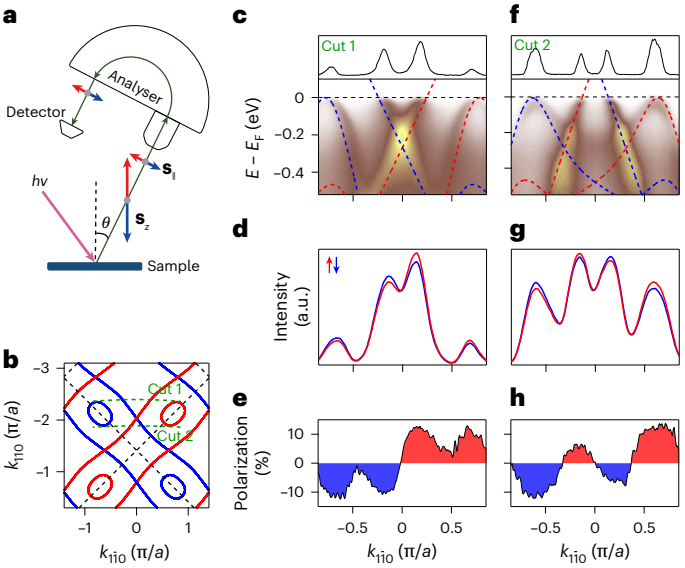

Fig. 3 | SARPES data. a, Schematic illustration of the geometry in the SARPES experiments. $\mathbf{S}_z$ denotes the spin polarization in the electronic structure of KV_2Se_2O, which is perpendicular to the (001) sample surface. θ is the angle between the normal direction of the sample surface and the emission direction of photoelectrons. $\mathbf{S}_\parallel$ denotes the in-plane projection $\mathbf{S}_\parallel = \mathbf{S}_z \sin\theta$, which can be detected by the spin detector. **b**, Calculated spin-resolved FSs at $k_z = 0$ with green dashed lines indicating the momentum locations of cuts 1 and 2 in the BZ. **c**,**f**, ARPES intensity plots showing the band dispersion along cut 1 (**c**) and along cut 2 (**f**). Red and blue dashed curves are calculated spin-up and spin-down bands. The black curves are the MDCs at E_F. **d**,**g**, Spin-resolved MDCs at E_F along cut 1 (**d**) and along cut 2 (**g**). Red and blue curves are spin-up and spin-down signals. **e**,**h**, Momentum-dependent spin polarizations calculated by the asymmetry of the spin-up and spin-down signals in **d** (**e**) and **g** (**h**). Red and blue filled areas highlight the spin-up and spin-down polarizations. All data in this figure were collected at 20 K with $h\nu = 67$ eV under linear vertical polarization.

with a d-wave form in electronic bands[1,2]. As schematically illustrated in Fig. 1c, the bands along [100] and [010] exhibit opposite spin-splitting, corresponding to the same $[C_2||C_{4z}]$ symmetry operation in real space. By contrast, the bands are spin degenerate along [110] enforced by the $[C_2||M_{1\bar{1}0}]$ symmetry, where $M_{1\bar{1}0}$ represents a mirror operation about the $(1\bar{1}0)$ plane.

Band structure with d-wave spin-splitting

Based on the magnetic structure in Fig. 1a, we calculated the electronic structure of KV_2Se_2O. Figure 2a displays the spin-resolved FSs in the three-dimensional (3D) Brillouin zone (BZ), which consist of quasi-one-dimensional (1D) FS sheets extending along the k_x and k_y directions and quasi-two-dimensional (2D) FS pockets at the BZ boundary. These FSs originate from opposite-spin 3*d* orbitals of the $V_\uparrow$ and $V_\downarrow$ sublattices. Orbital- and spin-resolved band calculations indicate that the crystal fields lift the degeneracy of the V 3*d* orbitals, which have opposite spin-splitting corresponding to the opposite-spin sublattices (Extended Data Fig. 2). The spin-up d_{xz} orbital of $V_\uparrow$ and spin-down d_{yz} orbital of $V_\downarrow$ were nearly half-filled. Owing to their strong in-plane anisotropy, the bands derived from these two orbitals form the quasi-1D FS sheets. The bands associated with the spin-up d_{xy} orbital of $V_\uparrow$ and spin-down d_{xy} orbital of $V_\downarrow$ are nearly fully occupied. They form the small quasi-2D FS pockets, as the d_{xy} orbital is more isotropic in the *a*–*b* plane. Comparing the band structures at $k_z = 0$ and π reveals weak k_z dispersion near E_F (Extended Data Fig. 3b). By contrast, the bands around −1 eV show moderate k_z dispersion because of the contribution from the d_{z^2} orbital, which has stronger out-of-plane coupling. Overall, the band structure of KV_2Se_2O has a nearly 2D nature, consistent with the photon energy ($h\nu$)-dependent ARPES results (Extended Data Fig. 3c), reflecting the weak interlayer coupling in its layered crystal structure.

The band calculations without SOC show identical dispersion but opposite spin-splitting along Γ–X–M and Γ–Y–M, whereas the bands along Γ–M remain spin degenerate (Fig. 2d), illustrating d-wave spin-splitting in the altermagnetic phase of KV_2Se_2O. When SOC is included, small gaps appear at the intersections along Γ–X–M and Γ–Y–M, whereas the band degeneracy along Γ–M is preserved (Extended Data Fig. 4). The degeneracy is lifted when deviating from $k_z = 0$ and π (Extended Data Fig. 5). However, the splitting is minimal due to the weak SOC in the V 3*d* orbitals, making the effects of SOC on the d-wave exchange splitting negligible.

The altermagnetic spin-splitting arises from the anisotropic crystal fields of ligand O and Se atoms. The anisotropy of crystal fields leads to band anisotropy between Γ–X–M and Γ–Y–M. Because of the C_{4z} rotation symmetry, the bands along Γ–X–M of one sublattice correspond to those along Γ–Y–M of the other sublattice. As the bands of the two sublattices have opposite spin polarizations, the band anisotropy results in momentum-dependent spin-splitting between them. The spin-splitting across E_F reaches a maximum of 1.6 eV at the X and Y points, as indicated by the green arrow in Fig. 2d, which is one of the highest values reported for altermagnetic materials. This notable spin-splitting is associated with the $V_\uparrow$ d_{xz} and $V_\downarrow$ d_{yz} orbitals, which form highly anisotropic bonds in the *a*–*b* plane. The anisotropy in bonding enhances the band anisotropy, leading to the large altermagnetic spin-splitting (Extended Data Fig. 6).

These calculated results are in good agreement with the measured FSs and band dispersions (Fig. 2c,e). We compared the ARPES data taken at 20 K with the calculated bands in Fig. 2e, as the spectral features are much clearer at low temperatures. The band dispersions at 20 K are largely consistent with those at 120 K (Extended Data Fig. 8). The extra feature near the M point along X–M and the gap opening at E_F on some bands at 20 K arise from the SDW order, which will be discussed below. Furthermore, the strong intensity midway between Γ and M aligns more closely with the calculations at $k_z = \pi$ (Extended Data Fig. 3d). The excellent agreement between the experimental and calculated results strongly supports the magnetic structure with altermagnetic order in KV_2Se_2O.

To verify the spin polarization of the band structure, we conducted SARPES experiments. As the NMR data reveal that the spins align along the *c* axis, the spin polarization $\mathbf{S}_z$ in the band structure was parallel to the normal direction of the (001) sample surface. In the experimental set-up, schematically illustrated in Fig. 3a, the spin detector can measure the in-plane spin polarization $\mathbf{S}_\parallel$. As the samples were rotated away from the normal direction by an angle θ, the spin polarization $\mathbf{S}_z$ has an in-plane projection $\mathbf{S}_\parallel = \mathbf{S}_z \sin\theta$. To enhance the in-plane projection, we measured momentum cuts in higher BZs by rotating the samples at larger angles.

Figure 3b shows the momentum locations of two measured cuts that pass through four representative spin-polarized FSs in the BZ. The spin polarizations follow a down-down-up-up sequence along cut 1. Moving towards cut 2, two quasi-1D FSs with opposite spin polarizations cross each other, resulting in a switch of their positions. Consequently, the spin polarizations change to a down-up-down-up sequence along cut 2. The spin-integrated ARPES spectra along the two cuts have two hole-like bands with their tops close to E_F (Fig. 3c,f), indicating that these cuts are nearly tangent to the hole-like FS pockets. Additionally, two nearly linear bands intersect below E_F along cut 1, whereas the intersection point shifts above E_F along cut 2. This results in a switch of their k_F positions, corresponding to the intersection of the quasi-1D FSs in Fig. 3b.

Then, we measured the spin polarizations of the ARPES spectra near E_F along the two cuts. The spin-up and spin-down momentum distribution curves (MDCs) at E_F have four peaks (Fig. 3d,g), corresponding to four spin-polarized FSs. These peaks exhibit clear intensity differences between the spin-up and spin-down MDCs, confirming the existence of spin polarization. Figure 3e,h shows that the spin polarizations have down-down-up-up and down-up-down-up sequences along cuts 1 and 2, respectively, in agreement with the calculations. The maximum spin polarization in the spectra is about 10%. As the samples were rotated by 26° and 22° for cuts 1 and 2, respectively, the in-plane projection $\mathbf{S}_\parallel = \mathbf{S}_z \sin\theta \approx 0.4\mathbf{S}_z$. As calibration, we measured the spin polarizations of the topological surface state of Bi_2Se_3, which is fully in-plane spin-polarized due to spin-momentum locking. The spectra have a maximum spin polarization of about 30% for Bi_2Se_3 (Extended Data Fig. 9). Given the 40% in-plane projection in the experiments with KV_2Se_2O, the maximum value of 10% is consistent with the spin polarizations along the *z* axis in the bands. These results reveal that the spin polarizations along the two cuts is antisymmetric with respect to the nodal line Γ–M, providing solid evidence for the altermagnetic order with an unconventional d-wave spin texture in KV_2Se_2O.

Another SDW order

Next, we analyse the electronic structure in the SDW phase below 100 K. Figure 4b,c displays the band dispersions along Γ–X and Y–M at 20 K. The bands labelled α, β, γ and δ are consistent with the calculations in Fig. 2d. In addition to these original bands, extra bands (α′, γ′ and δ′) are observed near E_F. The dispersions of these extra bands match those of the original bands α, γ and δ, except for a shift of π/a along the k_x direction, indicating band folding with a wavevector $\mathbf{q} = (\pi/a, \pi/a)$. The folded band α′(γ′) intersects the original band γ(α) at E_F, where a hybridized gap opens. The α and γ bands are associated with the quasi-1D FSs, which are perfectly nested through $\mathbf{q} = (\pi/a, \pi/a)$ (Fig. 4d). Figure 4e shows the symmetrized energy distribution curves (EDCs) at different momentum locations on the quasi-1D FSs, which exhibit a uniform gap size across the FSs. The temperature-dependent symmetrized EDCs indicate that the gap remained well above the SDW transition temperature, although the coherent peak disappeared (Fig. 4f). The pseudogap-like behaviour may arise from strong phase fluctuations above the SDW transition. By contrast, the poorly nested FS pockets at the X and Y points remained gapless in the SDW phase, indicating a metallic ground state (Extended Data Fig. 10). These results reveal that FS nesting plays an important role in the SDW transition.

Under the band folding with $\mathbf{q} = (\pi/a, \pi/a)$, the in-plane period becomes $\sqrt{2}a \times \sqrt{2}a$. In the SDW phase, the zero-field NMR spectra

https://doi.org/10.1038/s41567-025-02822-y

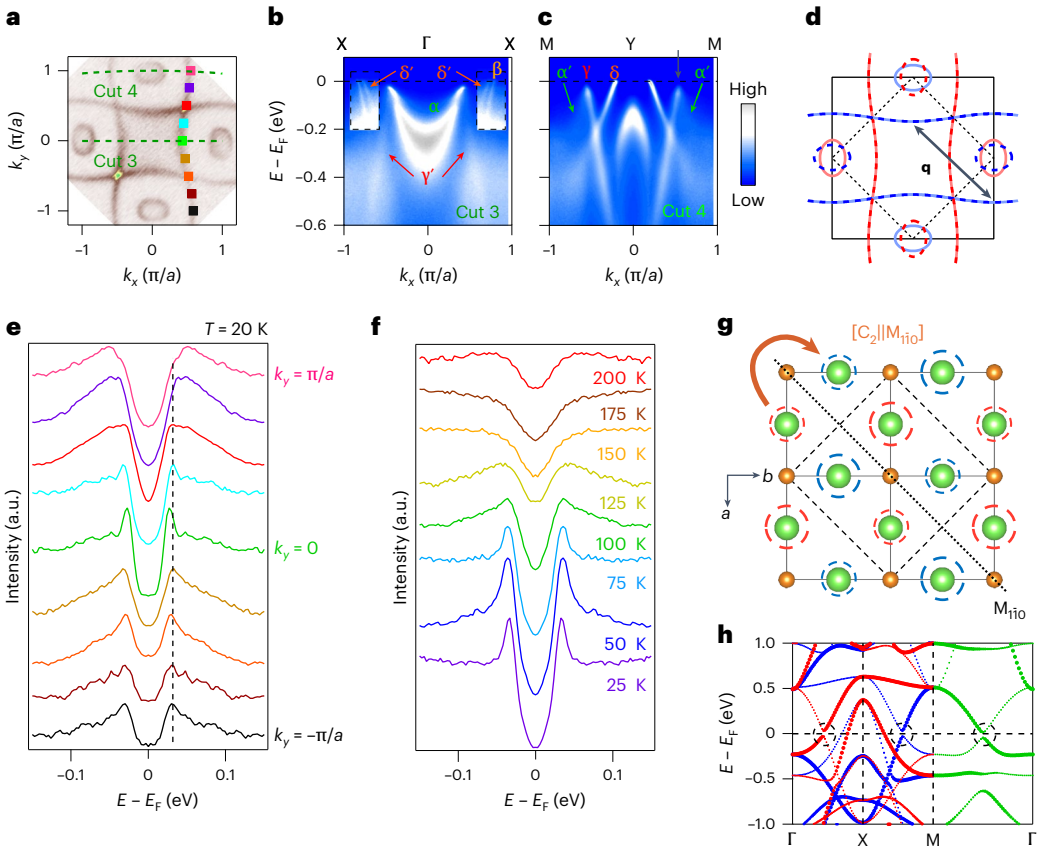

Fig. 4 | Electronic structure in the SDW phase. a, ARPES intensity plot at E_F showing FSs in the k_x–k_y plane. The green dashed lines indicate the momentum locations of cuts 3 and 4 in the BZ. **b**,**c**, ARPES intensity plots showing band dispersions along cut 3 (**b**) and cut 4 (**c**). α, β, γ and δ denote the original bands, whereas α′, γ′ and δ′ denote the bands folded from α, γ and δ. The colour scale in the dashed box in **b** is adjusted to enhance the bands near the X point. **d**, Original FSs (solid curves) extracted from the data in **a** with folded FSs (dashed curves) by **q** = (π/*a*, π/*a*). The black dashed lines indicate the reconstructed BZ in the SDW phase. **e**, Symmetrized EDCs at 20 K at different k_F points of the quasi-1D FS, whose positions are marked by squares in **a**. **f**, Symmetrized EDCs at the k_F point of the quasi-1D FS (marked by the black arrow in **c**) at different temperatures. **g**, Top view of the V_2O plane in the SDW phase. Red and blue dashed circles surrounding the V atoms denote up and down spins. The size of the dashed circles represents the magnitudes of the magnetic moments. The black dashed lines indicate one unit cell in the SDW phase. The black dotted line indicates the $M_{1\bar{1}0}$ mirror plane. Two opposite-spin sublattices are connected by the $[C_2||M_{1\bar{1}0}]$ operation in the SDW phase. **h**, Calculated spin-resolved band structure along Γ–X–M–Γ in the SDW phase. The size of the dots scales the spectra weight from the calculations. The black dashed circles highlight the gap opening at E_F. The data in **a** and **f** were collected with $h\nu$ = 67 eV whereas those in **b**, **c** and **e** were collected with $h\nu$ = 36 eV.

have two sets of peaks, indicating two distinct magnitudes of the magnetic moments. Each set of peaks further splits into two under a magnetic field along the *c* axis (Fig. 1d), revealing that the magnetic moments of each magnitude have opposite spins aligned along the *c* axis. Based on these results, we propose a magnetic structure in the SDW phase, as depicted in Fig. 4g. The calculations based on this structure indicate that the band folding opens a sizeable gap in the quasi-1D FSs (Fig. 4h), consistent with the experimental observations. In the SDW phase, the opposite-spin sublattices are connected by the spin group symmetry $[C_2||M_{1\bar{1}0}]$ (Fig. 4g). Therefore, KV_2Se_2O maintains its altermagnetism in the SDW phase.

Summary and outlook

Through a systematic characterization and analysis of the magnetic and electronic structures of KV_2Se_2O, we have unambiguously demonstrated the existence of altermagnetic order with d-wave spin-splitting in the electronic bands. As a metallic room-temperature altermagnet with highly anisotropic C_2-symmetry spin-polarized FSs, KV_2Se_2O holds remarkable potential for spintronic applications. Given the anti-CuO_2 structure of the V_2O plane, the d-wave altermagnet KV_2Se_2O is structurally compatible with d-wave cuprate superconductors, thus paving the way for uncovering previously unknown physics at the interfaces of unconventional superconductors and altermagnets[45–48]. The emergence of an SDW order provides a unique opportunity for explore intriguing quantum phenomena induced by many-body interactions, such as unconventional superconductivity, in the context of altermagnetism. Furthermore, by extracting K atomic layers through the topochemical deintercalation method, an exfoliable 2D compound V_2Se_2O with a van der Waals structure can be synthesized[44], offering a promising platform for developing 2D spintronic devices based on altermagnetism.

Online content

Any methods, additional references, Nature Portfolio reporting summaries, source data, extended data, supplementary information, acknowledgements, peer review information; details of author contributions and competing interests; and statements of data and code availability are available at https://doi.org/10.1038/s41567-025-02822-y.

References

1. Šmejkal, L., Sinova, J. & Jungwirth, T. Beyond conventional ferromagnetism and antiferromagnetism: a phase with nonrelativistic spin and crystal rotation symmetry. *Phys. Rev. X* **12**, 031042 (2022).

2. Šmejkal, L., Sinova, J. & Jungwirth, T. Emerging research landscape of altermagnetism. *Phys. Rev. X* **12**, 040501 (2022).
3. Šmejkal, L., MacDonald, A. H., Sinova, J., Nakatsuji, S. & Jungwirth, T. Anomalous Hall antiferromagnets. *Nat. Rev. Mater.* **7**, 482–496 (2022).
4. Šmejkal, L., Hellenes, A. B., González-Hernández, R., Sinova, J. & Jungwirth, T. Giant and tunneling magnetoresistance in unconventional collinear antiferromagnets with nonrelativistic spin-momentum coupling. *Phys. Rev. X* **12**, 011028 (2022).
5. González-Hernández, R. et al. Efficient electrical spin splitter based on nonrelativistic collinear antiferromagnetism. *Phys. Rev. Lett.* **126**, 127701 (2021).
6. Ma, H.-Y. et al. Multifunctional antiferromagnetic materials with giant piezomagnetism and noncollinear spin current. *Nat. Commun.* **12**, 2846 (2021).
7. Liu, P., Li, J., Han, J., Wan, X. & Liu, Q. Spin-group symmetry in magnetic materials with negligible spin-orbit coupling. *Phys. Rev. X* **12**, 021016 (2022).
8. Naka, M. et al. Spin current generation in organic antiferromagnets. *Nat. Commun.* **10**, 4305 (2019).
9. Yuan, L.-D., Wang, Z., Luo, J.-W. & Zunger, A. Prediction of low-*Z* collinear and noncollinear antiferromagnetic compounds having momentum-dependent spin splitting even without spin-orbit coupling. *Phys. Rev. Mater.* **5**, 014409 (2021).
10. Reichlová, H. et al. Macroscopic time reversal symmetry breaking by staggered spin-momentum interaction. Preprint at arxiv.org/abs/2012.15651 (2020).
11. Šmejkal, L., González-Hernández, R., Jungwirth, T. & Sinova, J. Crystal time-reversal symmetry breaking and spontaneous Hall effect in collinear antiferromagnets. *Sci. Adv.* **6**, eaaz8809 (2020).
12. Brinkman, W. F. & Elliott, R. J. Theory of spin-space groups. *Proc. R. Soc. A.* **294**, 343 (1966).
13. Litvin, D. B. & Opechowski, W. Spin groups. *Physica* **76**, 538 (1974).
14. Litvin, D. B. Spin point groups. *Acta Crystallogr. Sect. A: Found. Adv.* **33**, 279 (1977).
15. Chen, X. et al. Enumeration and representation of spin space groups. *Phys. Rev. X* **14**, 031038 (2024).
16. Chen, X., Ren, J., Li, J., Liu, Y. & Liu, Q. Spin space group theory and unconventional magnons in collinear magnets. Preprint at arxiv.org/abs/2307.12366v1 (2023).
17. Xiao, Z., Zhao, J., Li, Y., Shindou, R. & Song, Z. D. Spin space groups: full classification and applications. *Phys. Rev. X* **14**, 031037 (2024).
18. Jiang, Y. et al. Enumeration of spin-space groups: towards a complete description of symmetries of magnetic orders. *Phys. Rev. X* **14**, 031039 (2024).
19. Yang, J., Liu, Z.-X. & Fang, C. Symmetry invariants and classes of quasi-particles in magnetically ordered systems having weak spin-orbit coupling. *Nat. Commun.* **15**, 10203 (2024).
20. Dresselhaus, G. Spin-orbit coupling effects in zinc blende structures. *Phys. Rev.* **100**, 580 (1955).
21. Rashba, E. Properties of semiconductors with an extremum loop. I. Cyclotron and combinational resonance in a magnetic field perpendicular to the plane of the loop. *Sov. Phys. Solid State* **2**, 1109 (1960).
22. Jungwirth, T., Marti, X., Wadley, P. & Wunderlich, J. Antiferromagnetic spintronics. *Nat. Nanotechnol.* **11**, 231 (2016).
23. Baltz, V. et al. Antiferromagnetic spintronics. *Rev. Mod. Phys.* **90**, 015005 (2018).
24. Shao, D. F., Zhang, S. H., Li, M., Eom, C. B. & Tsymbal, E. Y. Spin-neutral currents for spintronics. *Nat. Commun.* **12**, 7061 (2021).
25. Qin, P. et al. Room-temperature magnetoresistance in an all-antiferromagnetic tunnel junction. *Nature* **613**, 485 (2023).
26. Chen, X. et al. Octupole-driven magnetoresistance in an antiferromagnetic tunnel junction. *Nature* **613**, 490 (2023).
27. Krempaský, J. et al. Altermagnetic lifting of Kramers spin degeneracy. *Nature* **626**, 517 (2024).
28. Zhu, Y.-P. et al. Observation of plaid-like spin splitting in a noncoplanar antiferromagnet. *Nature* **626**, 523 (2024).
29. Osumi, T. et al. Observation of a giant band splitting in altermagnetic MnTe. *Phys. Rev. B* **109**, 115102 (2024).
30. Lee, S. et al. Broken Kramers degeneracy in altermagnetic MnTe. *Phys. Rev. Lett.* **132**, 036702 (2024).
31. Reimers, S. et al. Direct observation of altermagnetic band splitting in CrSb thin films. *Nat. Commun.* **15**, 2116 (2024).
32. Ding, J. et al. Large band-splitting in g-wave type altermagnet CrSb. *Phys. Rev. Lett.* **133**, 206401 (2024).
33. Yang, G. et al. Three-dimensional mapping of the altermagnetic spin splitting in CrSb. *Nat. Commun.* **16**, 1442 (2025).
34. Zeng, M. et al. Observation of spin splitting in room-temperature metallic antiferromagnet CrSb. *Adv. Sci.* **11**, 2406529 (2024).
35. Berlijn, T. et al. Itinerant antiferromagnetism in RuO_2. *Phys. Rev. Lett.* **118**, 077201 (2016).
36. Zhu, Z. H. et al. Anomalous antiferromagnetism in metallic RuO_2 determined by resonant X-ray scattering. *Phys. Rev. Lett.* **122**, 017202 (2019).
37. Bose, A. et al. Tilted spin current generated by the collinear antiferromagnet ruthenium dioxide. *Nat. Electron.* **5**, 267 (2022).
38. Bai, H. et al. Observation of spin splitting torque in a collinear antiferromagnet RuO_2. *Phys. Rev. Lett.* **128**, 197202 (2022).
39. Feng, Z. et al. An anomalous Hall effect in altermagnetic ruthenium dioxide. *Nat. Electron.* **5**, 735 (2022).
40. Karube, S. et al. Observation of spin-splitter torque in collinear antiferromagnetic RuO_2. *Phys. Rev. Lett.* **129**, 137201 (2022).
41. Lin, Z. et al. Observation of giant spin splitting and d-wave spin texture in room temperature altermagnet RuO_2. Preprint at arxiv.org/abs/2402.04995 (2024).
42. Hiraishi, M. et al. Nonmagnetic ground state in RuO_2 revealed by muon spin rotation. *Phys. Rev. Lett.* **132**, 166702 (2024).
43. Philipp, K. et al. Absence of magnetic order in RuO_2: insights from μSR spectroscopy and neutron diffraction. *npj Spintron.* **2**, 50 (2024).
44. Lin, H. et al. Structure and physical properties of $CsV_2Se_{2-x}O$ and V_2Se_2O. *Phys. Rev. B* **98**, 075132 (2018).
45. De Luca, G. M. et al. Ubiquitous long-range antiferromagnetic coupling across the interface between superconducting and ferromagnetic oxides. *Nat. Commun.* **5**, 5626 (2014).
46. Mazin, I. I., Golubov, A. A. & Nadgorny, B. Probing spin polarization with Andreev reflection: a theoretical basis. *J. Appl. Phys.* **89**, 7576 (2001).
47. Flensberg, K., von Oppen, F. & Stern, A. Engineered platforms for topological superconductivity and Majorana zero modes. *Nat. Rev. Mater.* **6**, 944 (2021).
48. Zhang, F. et al. Crystal-symmetry-paired spin-valley locking in a layered room-temperature antiferromagnet. Preprint at arxiv.org/abs/2407.19555 (2024).

Methods

Sample synthesis and characterization

KV_2Se_2O single crystals were grown using KSe as the self-flux agent. The K:V:Se:O molar ratio of the initial mixture was 6:2:7:1. The reactants were first sealed in a Nb tube, which was then jacketed with an evacuated quartz ampule and loaded into an alumina crucible. The quartz ampule was heated at 1,000 °C for 20 h and then gradually cooled to 650 °C at a rate of 2 K h^{-1} before the furnace was switched off. The samples obtained were black and sensitive to air and moisture.

The d.c. magnetization measurements were performed on a superconducting quantum interference device with a vibrating sample magnetometer (Quantum Design). Several pieces of single crystal were used, and the background signal of the sample holder was deduced. The temperature-dependent magnetic susceptibility of KV_2Se_2O was measured in zero-field-cooling and field-cooling modes with the magnetic field $\mu_0 H$ applied parallel to the c axis and a–b plane, respectively. The magnetic field dependence of the magnetization of KV_2Se_2O was measured with $\mu_0 H$ up to 7 T.

NMR spectroscopy

NMR measurements were carried out using a commercial NMR spectrometer from Thamway Co. Ltd. The NMR spectra were acquired by integrating the intensity of the spin echo at each frequency. ^{51}V with nuclear spin $I = 7/2$ has seven NMR peaks due to quadrupole splitting. At high temperatures, the satellite peaks are higher than the central peak. Such behaviour has been observed in NaV_2O_5 at 34 K (ref. 49). The internal fields were calculated using $B_{in} = f/\gamma$, where f is the frequency and the gyromagnetic ratio $\gamma = 11.19913$ MHz T^{-1}. As the internal field at the ^{51}V position comes primarily from its own electrons, the hyperfine coupling constant should be like that of other vanadium materials. The magnetic moments were estimated with $M = B_{in}/A_{AF}$, where the hyperfine coupling constant $A_{AF} = 16$ T/μ_B is the value for $LaVO_3$ and V_2O_3 (ref. 50) and μ_B is the Bohr magneton.

The T_1 values were measured by using a single saturating pulse and were determined by standard fits to the recovery curves of the nuclear magnetization to the theoretical function for the nuclear spin $I = 7/2$. The central peak was fitted by

$$\frac{M(\infty)-M(t)}{M(\infty)} = \frac{1}{84}\exp\left(-\frac{t}{T_1}\right) + \frac{3}{44}\exp\left(-\frac{6t}{T_1}\right) + \frac{75}{364}\exp\left(-\frac{15t}{T_1}\right) + \frac{1{,}225}{1{,}716}\exp\left(-\frac{28t}{T_1}\right),$$

and the third satellite peak was fitted by

$$\frac{M(\infty)-M(t)}{M(\infty)} = \frac{1}{84}\exp\left(-\frac{t}{T_1}\right) + \frac{3}{28}\exp\left(-\frac{3t}{T_1}\right) + \frac{3}{11}\exp\left(-\frac{6t}{T_1}\right) + \frac{25}{77}\exp\left(-\frac{10t}{T_1}\right) + \frac{75}{364}\exp\left(-\frac{15t}{T_1}\right) + \frac{3}{44}\exp\left(-\frac{21t}{T_1}\right) + \frac{4}{429}\exp\left(-\frac{28t}{T_1}\right),$$

where $M(t)$ is the nuclear magnetization at time t after the saturation pulse.

Neutron diffraction

Neutron powder diffraction measurements was conducted at the general-purpose powder diffractometer (GPPD) at the China Spallation Neutron Source. The GPPD is a time-of-flight diffractometer with a neutron bandwidth of 4.8 Å, and it provides a maximum resolution $\Delta d/d = 0.15\%$. The neutron pattern data in this study were acquired from three different banks of GPPD: 150° bank, 90° bank and 30° bank, which correspond to the central solid angles of the detector being $2\theta = 150°$, 90° or 30°, respectively. The d-space range for data obtained from the 150° bank was between 0.05 and 2.7 Å, for data obtained from the 90° bank it was between 0.06 and 4.3 Å, and for data obtained from the 30° bank it was between 0.12 and 28.11 Å. The sample under investigation was loaded into TiZr cans. The diameter of each can was approximately 9 mm. All measurements were performed at room temperature. The diffraction profiles were analysed by Rietveld refinement with the FULLPROF suite/GSAS.

X-ray diffraction

Single crystal X-ray diffraction measurements were performed by using the custom-designed X-ray instrument at 80 K. It was equipped with a Xenocs Genix3D Mo Kα X-ray source (17.48 keV), which provided 2.5×10^7 photons per second in a beam spot size of 150 μm at the sample position. The measured samples were mounted on a Huber four-circle diffractometer. Diffraction signals were collected by a highly sensitive single-photon counting PILATUS3 R 1M solid-state area detector with 980 × 1,042 pix^2. Each pixel was 172 μm × 172 μm. The 3D mapping of momentum space was obtained by taking images in 0.1° increments while rotating the samples.

ARPES

ARPES measurements were performed at the dreamline (BL09U) beamline and the BL03U beamline of the Shanghai Synchrotron Radiation Facility using a Scienta Omicron DA30L electron analyser under both linear vertical and linear horizontal polarized incident light. The data were collected over a photon energy range 25 to 80 eV. The samples were cleaved in situ under a base pressure better than 5×10^{-11} mbar. SARPES measurements were carried out using the Scienta Omicron DA30L electron analyser and a single very-low-energy electron diffraction spin detector. The spin detection direction was perpendicular to the entrance slit.

Density functional theory calculations

The first-principles calculations were performed using the Vienna ab initio simulation package[51], with the generalized gradient approximation of Perdew–Burke–Ernzerhof[52] type used as the exchange-correlation potential. SOC was not taken into account because of its minor influence on the band structure and the preservation of spin as a good quantum number in collinear magnetic structures without SOC. In the self-consistent calculation, a Monkhorst–Pack (9 × 9 × 5) k-point mesh[53] and an energy cutoff of 600 eV were used. To get the tight-binding model Hamiltonian, we used the package wannier90 (refs. 54,55) to obtain maximally localized Wannier functions of V d orbitals, Se p orbitals and O p orbitals.

To induce the SDW phase, we expanded the unit cell of the original magnetic structure by a factor of $\sqrt{2} \times \sqrt{2}$ without altering the atomic positions. To investigate the resulting magnetic moments, we applied small correlation effects (with $U = 1.0$ eV)[56,57] to one pair of V atoms, one spin-up and the other spin-down. For direct comparison with the ARPES experiments, we conducted a band-unfolding procedure[58,59] to obtain the effective band structure in the BZ before enlarging the cell.

Data availability

All the data are available from the corresponding authors upon reasonable request. Source data are provided with this paper.

References

49. Ohama, T., Yasuoka, H., Isobe, M. & Ueda, Y. Mixed valency and charge ordering in α′–NaV_2O_5. *Phys. Rev. B* **59**, 3299 (1999).
50. Kikuchi, J., Yasuoka, H., Kokubo, Y. & Ueda, Y. Antiferromagnetic nuclear resonance of ^{51}V in $LaVO_3$ and YVO_3. *J. Phys. Soc. Jpn* **63**, 3577 (1994).
51. Kresse, G. & Furthmüller, J. Efficient iterative schemes for ab initio total-energy calculations using a plane-wave basis set. *Phys. Rev. B* **54**, 11169 (1996).

52. Perdew, J. P., Burke, K. & Ernzerhof, M. Generalized gradient approximation made simple. *Phys. Rev. Lett.* **77**, 3865 (1996).
53. Monkhorst, H. J. & Pack, J. D. Special points for Brillouin-zone integrations. *Phys. Rev. B* **13**, 5188 (1976).
54. Marzari, N. & Vanderbilt, D. Maximally localized generalized Wannier functions for composite energy bands. *Phys. Rev. B* **56**, 12847 (1997).
55. Mostofi, A. A. et al. wannier90: a tool for obtaining maximally-localised Wannier functions. *Comput. Phys. Commun.* **178**, 685 (2008).
56. Anisimov, V. I., Zaanen, J. & Andersen, O. K. Band theory and Mott insulators: Hubbard *U* instead of Stoner *I*. *Phys. Rev. B* **44**, 943 (1991).
57. Dudarev, S. L., Botton, G. A., Savrasov, S. Y., Humphreys, C. J. & Sutton, A. P. Electron-energy-loss spectra and the structural stability of nickel oxide: an LSDA+U study. *Phys. Rev. B* **57**, 1505 (1998).
58. Popescu, V. & Zunger, A. Extracting *E* versus $\vec{k}$ effective band structure from supercell calculations on alloys and impurities. *Phys. Rev. B* **85**, 085201 (2012).
59. Ku, W., Berlijn, T. & Lee, C.-C. Unfolding first-principles band structures. *Phys. Rev. Lett.* **104**, 216401 (2010).

Acknowledgements

We thank J. Liu, W. Yu, R. Zhou and C. Fang for fruitful discussions. We thank L. Deng and S. Qiao for assistance with the SARPES experiments at the Shanghai Institute of Microsystem and Information Technology. This work was supported by the Ministry of Science and Technology of China (Grant Nos. 2022YFA1403800, 2023YFA1406100, 2022YFA1403903, 2022YFA1602800, 2021YFA1401903, 2022YFA1403400, 2021YFA1400401 and 2022YFA1403100), the National Natural Science Foundation of China (Grant Nos. U22A6005, 11925408, 11921004, 12134018, 12188101, 12204222, 12204297, 12274440 and 12374143), the Chinese Academy of Sciences (Grant No. XDB33000000), the K. C. Wong Education Foundation (Grant No. GJTD-2020-01), the Zhejiang Provincial Natural Science Foundation of China (Grant No. LD24F040001) and the Synergetic Extreme Condition User Facility. We acknowledge the beam time at the GPPD granted by the China Spallation Neutron Source, at the BL09U and BL03U beamlines at the Shanghai Synchrotron Radiation Facility and at the Shanghai Institute of Microsystem and Information Technology. H.W. acknowledges support from the New Cornerstone Science Foundation through the Xplorer Prize. Y.H. acknowledges support from the Shanghai Municipal Science and Technology Major Project and the Shanghai Committee of Science and Technology (Grant No. 23JC1403300).

Author contributions

T.Q., H.W. and H.L. supervised the project. B.J., M.H., H.L. and T.Q. performed the ARPES and SARPES experiments with assistance from G.Q., Y.H. and W.L. J.B., W.Z. and G.C. synthesized the single crystals. Z.S., H.P. and H.W. performed the density functional theory calculations. C.M., Z.L. and J.L. performed the NMR experiments. L.H. and S.L. performed the neutron diffraction experiments. X.Z. and Y.P. performed the X-ray diffraction experiments. Z.W. and Y.S. performed the scanning tunnelling microscopy experiments. B.J., M.H., H.L. and T.Q. analysed the experimental data. B.J., M.H., Z.S., H.L. and T.Q. plotted the figures. T.Q. and H.L. wrote the manuscript with contributions from all authors.

Competing interests

The authors declare no competing interests.

Additional information

Extended data is available for this paper at https://doi.org/10.1038/s41567-025-02822-y.

Correspondence and requests for materials should be addressed to Zheng Li, Genfu Chen, Hang Li, Hongming Weng or Tian Qian.

Peer review information *Nature Physics* thanks the anonymous reviewers for their contribution to the peer review of this work.

https://doi.org/10.1038/s41567-025-02822-y

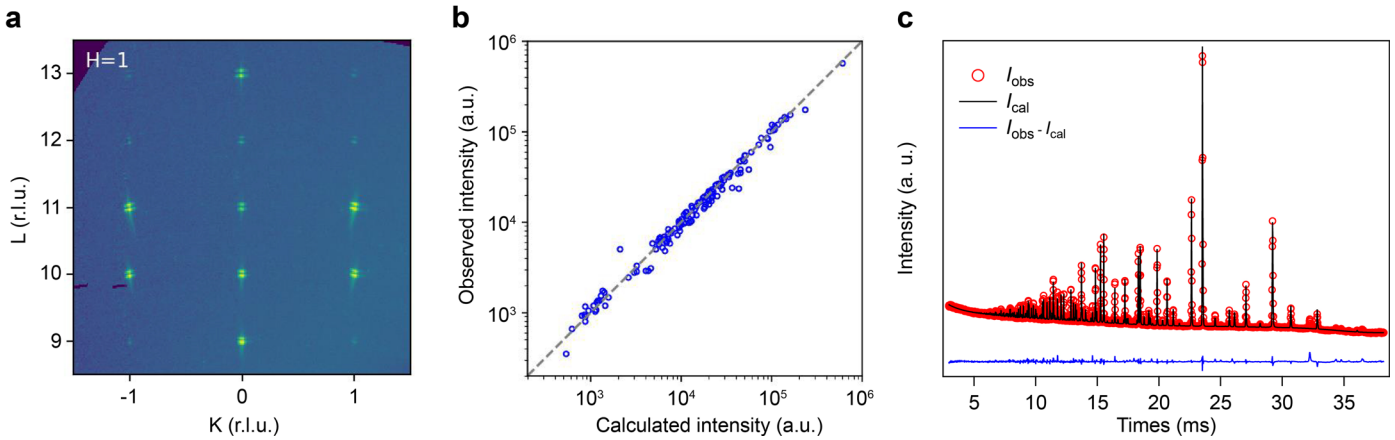

Extended Data Fig. 1 | Single crystal X-ray and powder neutron diffraction data. a, (*K*, *L*) map of reciprocal space at *H* = 1 measured at 80 K. The double peaks originate from the small non-monochromaticity of the Mo x-ray source, which consists of $K_{\alpha 1}$ (17.48 keV) and $K_{\alpha 2}$ (17.37 keV), and bremsstrahlung. The bright and sharp diffraction peaks indicate that the samples are of high quality with only one crystalline phase. **b**, Observed XRD intensities from 143 indexed Bragg peaks compared with the calculations based on the crystal structure with space group *P*4/*mmm*. **c**, Powder neutron diffraction spectrum at 300 K refined to the crystal structure with space group *P*4/*mmm*. The observed (Iobs) and calculated (Ical) patterns and the difference between them (I_{obs} - I_{cal}) are plotted.

https://doi.org/10.1038/s41567-025-02822-y

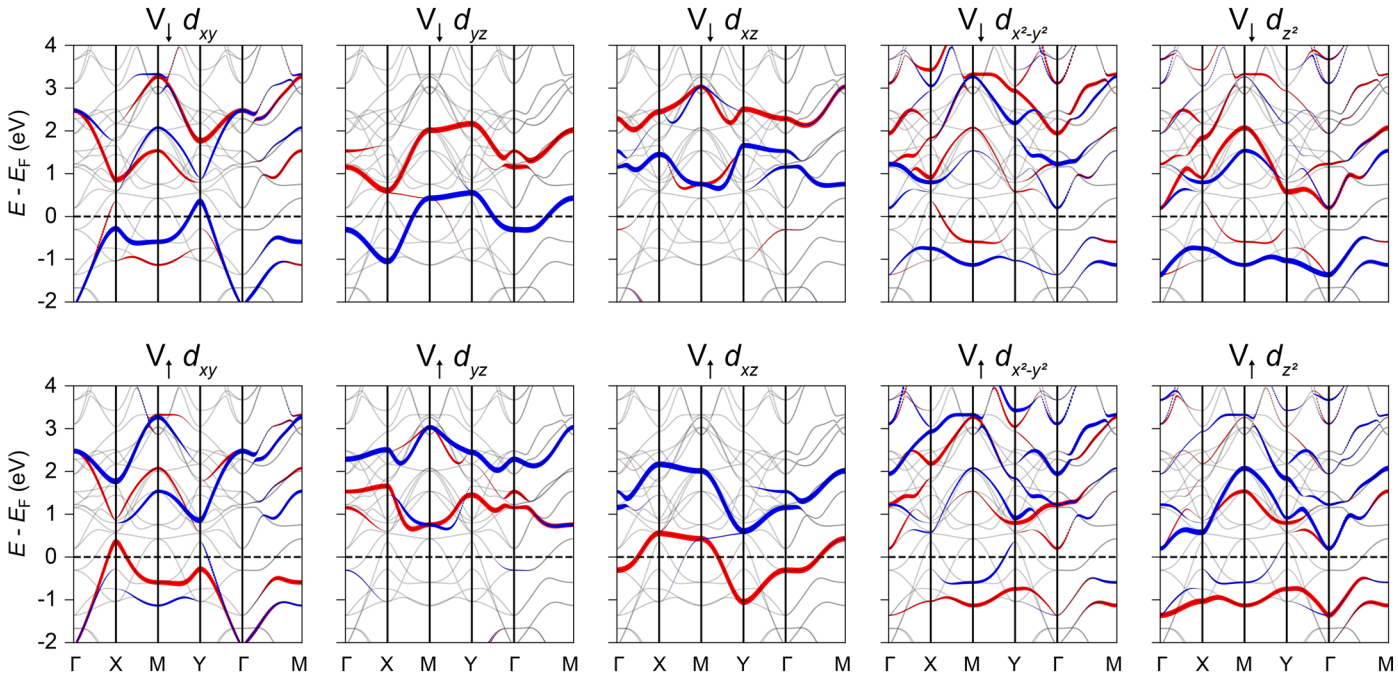

Extended Data Fig. 2 | Calculated orbital- and spin-resolved band structures along high-symmetry lines. Red and blue dots represent spin-up and spin-down bands. The size of the dots scales the projection of orbital components.

https://doi.org/10.1038/s41567-025-02822-y

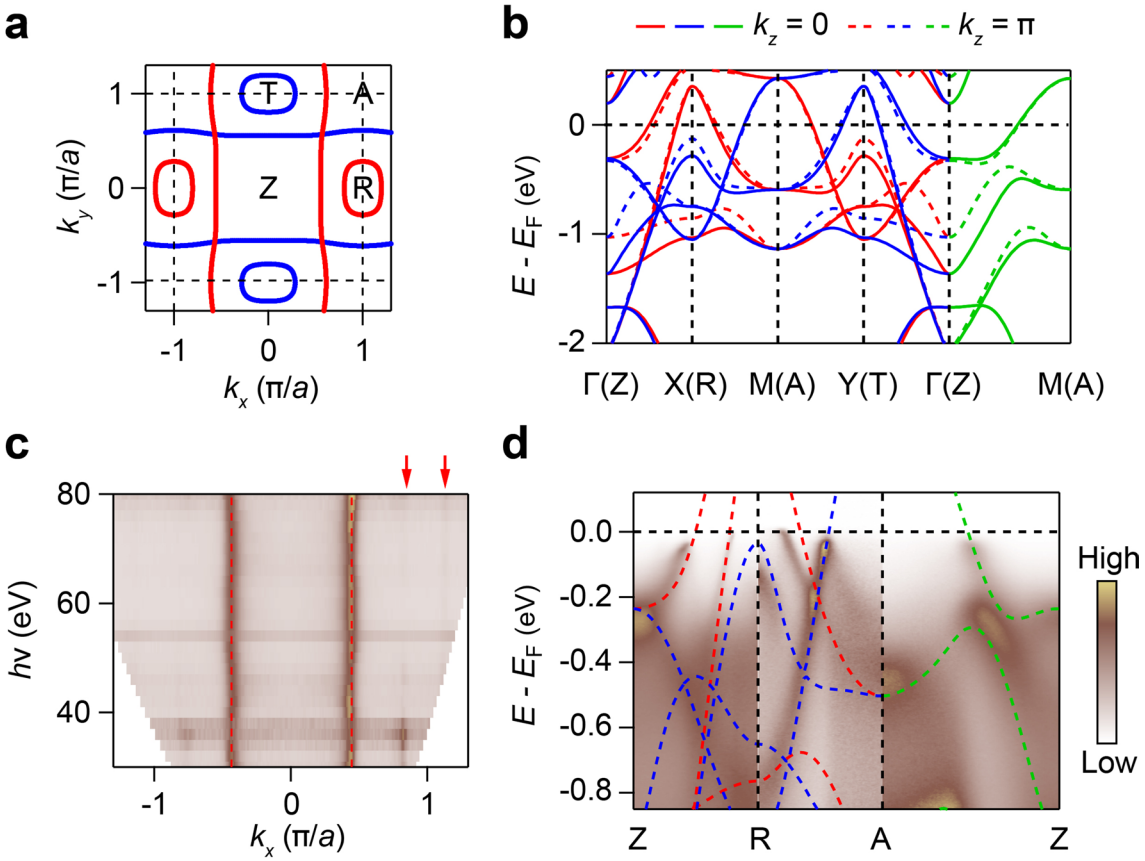

Extended Data Fig. 3 | Electronic structure in the 3D BZ. a, Calculated spin-resolved FSs at $k_z = \pi$. Red and blue curves are spin-up and spin-down FSs. Black dashed lines indicate the BZ boundary. **b**, Calculated spin-resolved band structure along high-symmetry lines at $k_z = 0$ (solid curve) and π (dashed curve). Red, blue, and green curves are spin-up, spin-down, and spin-degenerate bands. **c**, ARPES intensity plot at E_F measured along Γ–X with varying photon energy, showing FSs in the $k_y = 0$ plane. Vertical dashed lines and arrows indicate negligible k_z dispersion of the FSs. **d**, Comparison of the ARPES data taken at 20 K with the calculated bands at kz = π. The spectra are a sum of the data collected under LH and LV polarizations (Extended Data Fig. 8) with $h\nu = 67$ eV. Dashed curves are shifted upward by 90 meV for better matching the experimental data.

https://doi.org/10.1038/s41567-025-02822-y

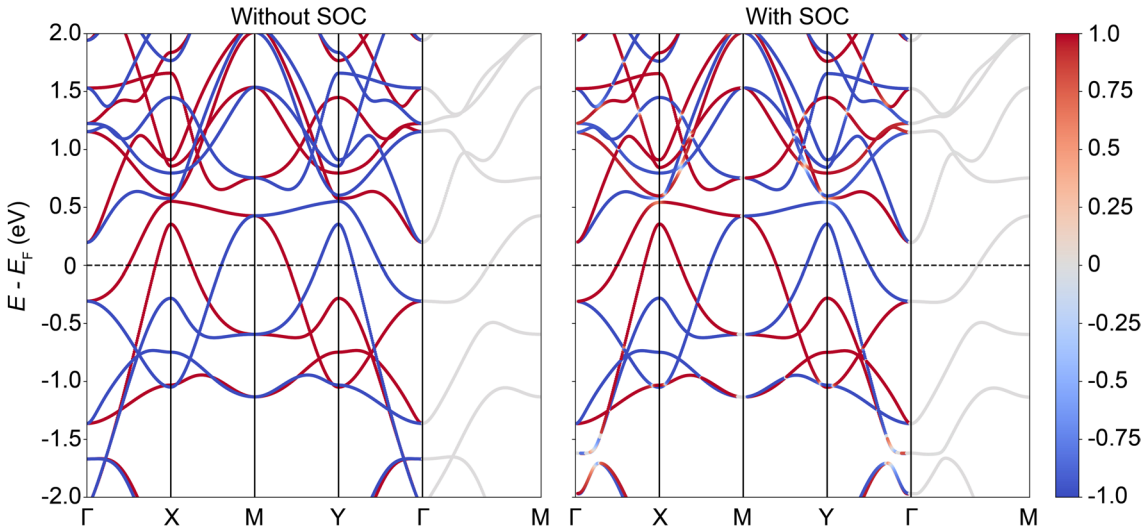

Extended Data Fig. 4 | Spin-resolved band structures at $k_z = 0$ without (left) and with (right) SOC. Opposite spin polarization components along the *c* axis are indicated by a red-blue color scale.

https://doi.org/10.1038/s41567-025-02822-y

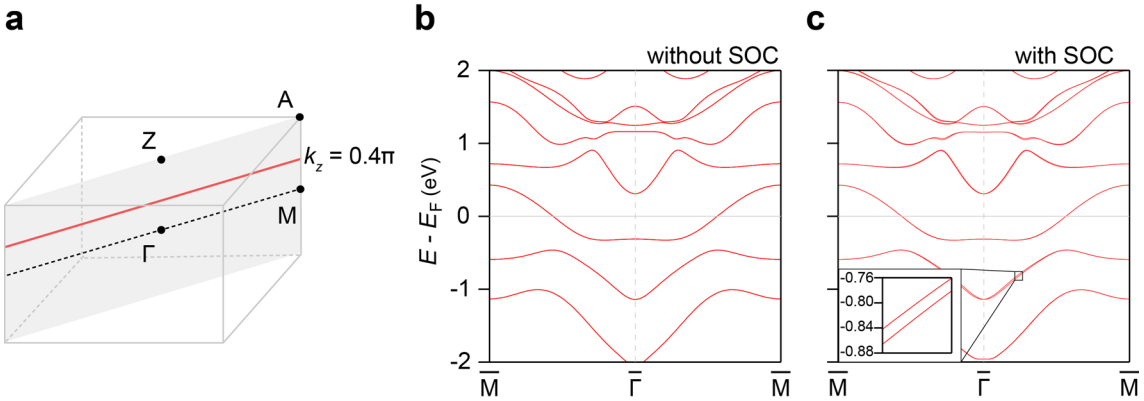

Extended Data Fig. 5 | Calculated band structures along $\bar{\Gamma} - \bar{M}$ at $k_z = 0.4\pi$ (red line in a) without (b) and with (c) SOC. The inset in **c** shows a zoom-in view of the bands within the black square.

https://doi.org/10.1038/s41567-025-02822-y

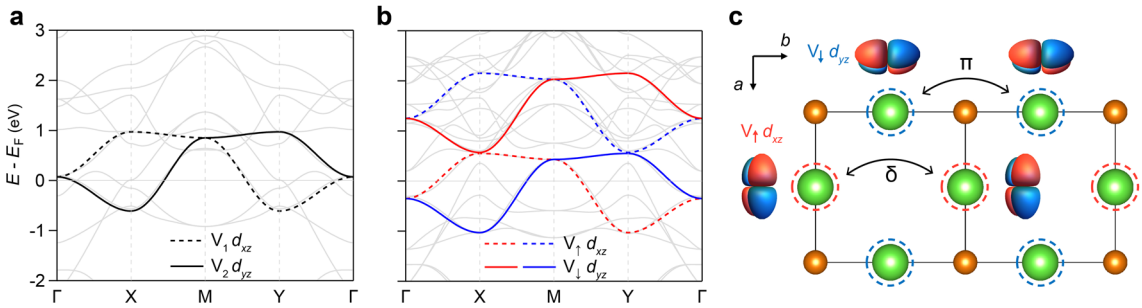

Extended Data Fig. 6 | Tight-binding calculations. a, Tight-binding calculations of the bands derived from the V_1 d_{xz} (dashed curves) and V_2 d_{yz} orbitals (solid curves) in the nonmagnetic phase. **b**, Tight-binding calculations of the bands derived from the $V_\uparrow$ d_{xz} (dashed curves) and the $V_\downarrow$ d_{yz} orbitals (solid curves) in the magnetically ordered phase. Red and blue represent spin-up and spin-down polarizations. **c**, Schematic of the $V_\uparrow$ d_{xz} and $V_\downarrow$ d_{yz} orbitals, which form δ and π bonds, respectively, along the *b* axis.

https://doi.org/10.1038/s41567-025-02822-y

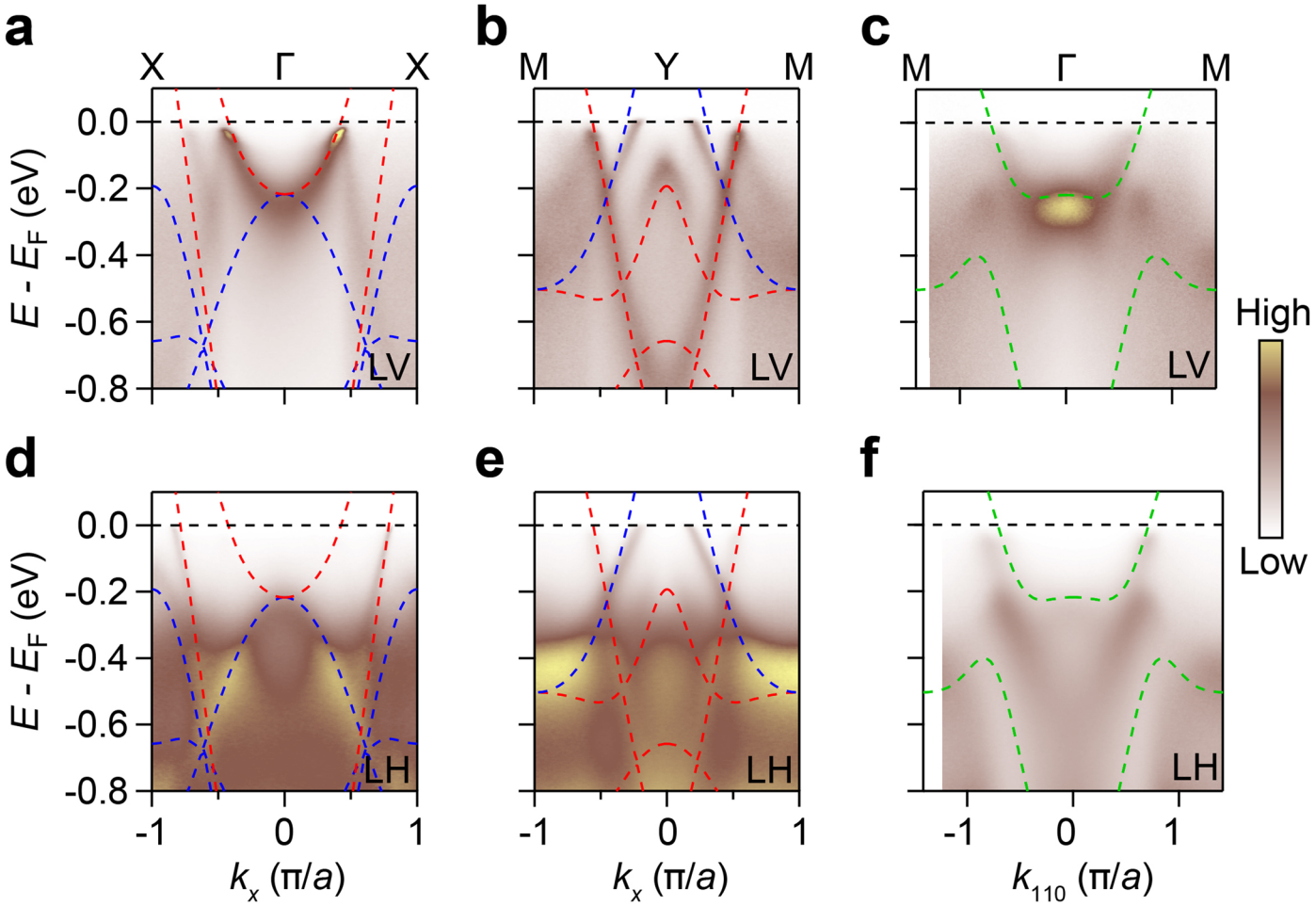

Extended Data Fig. 7 | Polarization-dependent ARPES data. a-c, ARPES intensity plots along Γ–X, Y–M and Γ–M measured at 20 K with $h\nu = 67$ eV under LV polarization. **d-f**, Same as **a-c** but measured with LH polarization. Red, blue, and green dashed curves are spin-up, spin-down, and spin-degenerate bands at $k_z = 0$.

https://doi.org/10.1038/s41567-025-02822-y

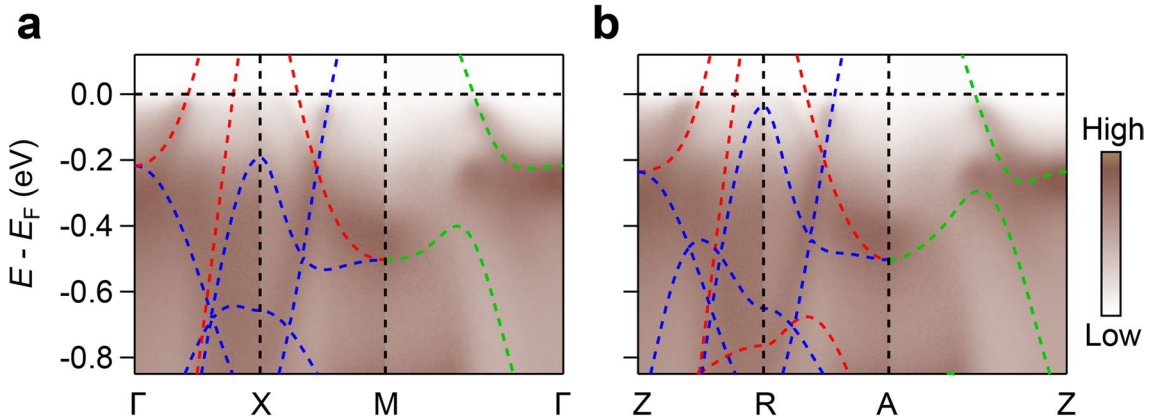

Extended Data Fig. 8 | Comparison of the ARPES data taken at 120 K with the calculated bands at $k_z = 0$ (a) and π (b). The ARPES spectra are a sum of the data collected under LH and LV polarizations with $h\nu = 67$ eV. Red, blue, and green dashed curves are spin-up, spin-down, and spin-degenerate bands.

https://doi.org/10.1038/s41567-025-02822-y

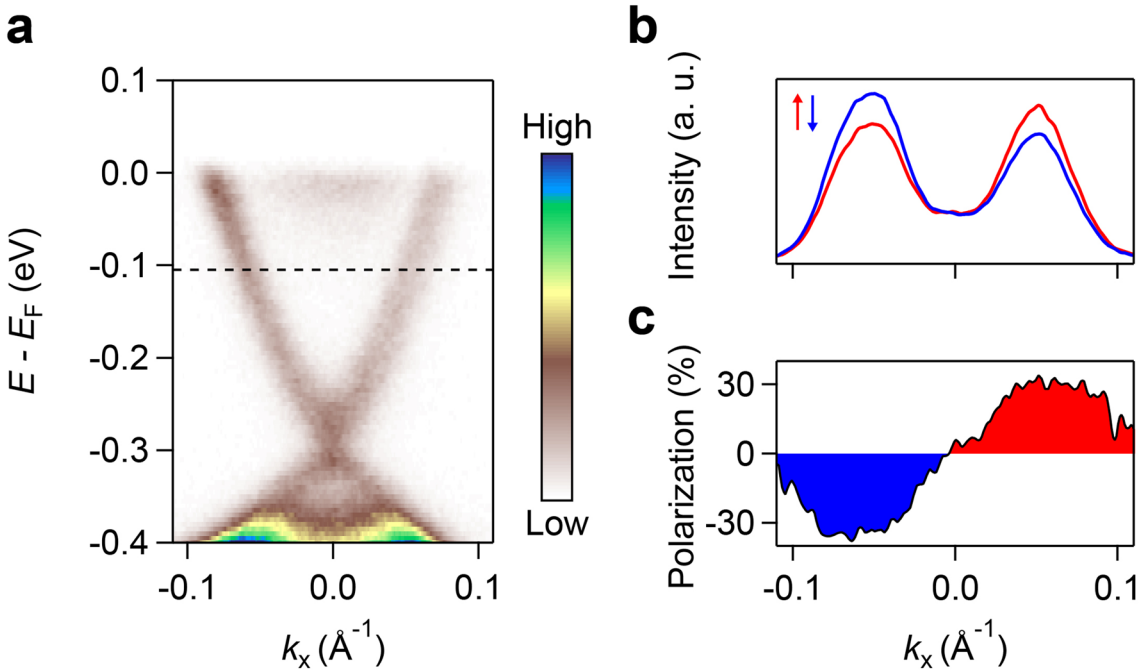

Extended Data Fig. 9 | Spin-resolved ARPES results of the topological surface state of Bi_2Se_3. a, ARPES intensity plot showing band dispersions across $\bar{\Gamma}$. **b**, Spin-resolved MDCs at an energy indicated by black dashed line in **a**. Red and blue curves are spin-up and spin-down signals. **c**, Momentum-dependent spin polarizations calculated by the asymmetry of the spin-up and spin-down signals in **b**. Red and blue filled areas highlight the spin-up and spin-down polarizations.

https://doi.org/10.1038/s41567-025-02822-y

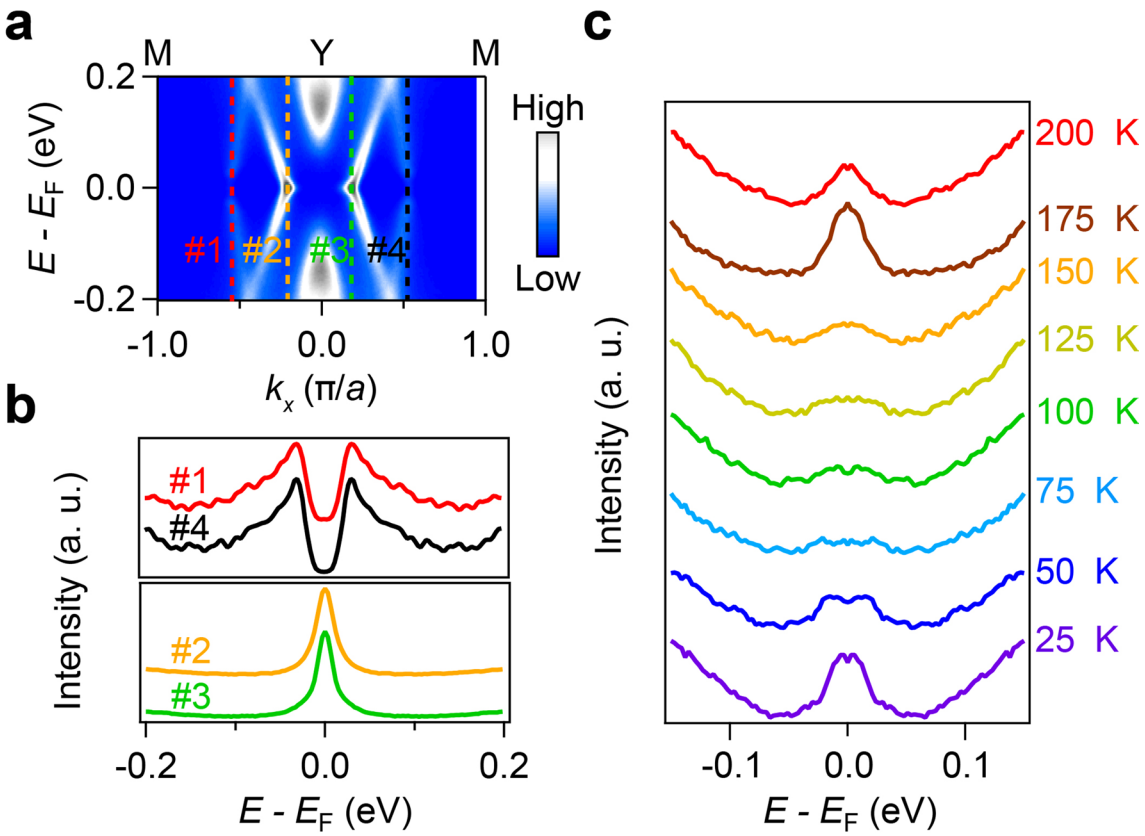

Extended Data Fig. 10 | Gapless FS pocket at the Y point. a, Symmetrized ARPES spectra along M–Y–M at 20 K. **b**, Symmetrized EDCs at 20 K at the k_F points marked by dashed lines in **a**. **c**, Symmetrized EDCs at the k_F point #3 in **a** at different temperatures.